Journal of Hazardous Materials 378 (2019) 120752

Contents lists available at ScienceDirect

Journal of Hazardous Materials

journal homepage: www.elsevier.com/locate/jhazmat

One–step reductive synthesis of Ti^{3+} self–doped elongated anatase TiO_2 nanowires combined with reduced graphene oxide for adsorbing and degrading waste engine oil

Dandan Cheng[a,b,1], Yaobang Li[a,b,1], Lixia Yang[a,b,*], Shenglian Luo[a,b,*], Liming Yang[a,b], Xubiao Luo[a,b], Yan Luo[a,b], Tingting Li[a,b], Jiong Gao[c], Dionysios D. Dionysiou[c]

[a] High Level Laboratory of Jiangxi Province for Persistent Pollutants Control, Recycle and Reuse, Nanchang Hangkong University, Nanchang, 330063, PR China
[b] College of Environmental and Chemical Engineering, Nanchang Hangkong University, Nanchang, 330063, PR China
[c] Environmental Engineering and Science Program, Department of Chemical and Environmental Engineering (DChEE), 705 Engineering Research Center, University of Cincinnati, Cincinnati, OH, USA

GRAPHICAL ABSTRACT

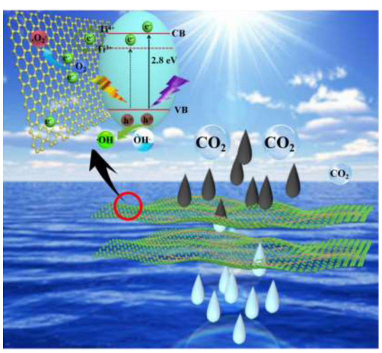

ARTICLE INFO

Keywords:
Elongated anatase TiO_2 nanowires
TiO_2 NWs@rGO composites
Ti^{3+} self–doped
Photocatalysis
Self–cleaning

ABSTRACT

A sustainable photocatalyst of Ti^{3+} self–doped elongated anatase nanowires combined with reduced graphene oxide (TiO_2 NWs@rGO) was prepared via a facile one–step reductive synthesis process using $NaBH_4$ as reductant for the first time. The obtained optimal TiO_2 NWs@rGO composite has a large surface area,182 m^2 g^{-1}, which demonstrates strong adsorption capacity due to the multilayered structure built by highly crystallized nanowires of TiO_2 and ultrathin rGO layers. When the photocatalyst was applied in removing waste engine oil (100 mL, 50 mg L^{-1}), it exhibited outstanding performance with up to COD 98.6% removal extent (from 145 initial to 2 mg L^{-1} final COD) after 5 h, which is 34.1% higher than that of TiO_2 NWs (64.5% COD removal extent). Gas chromatography–mass spectrometry analyses of residual waste engine oil after photocatalysis shows significant reductions of C_6–C_{19} chemicals as well as total disappear of C_{15},C_{16}, C_{17}, C_{18} chemicals. The outstanding photocatalytic activity of TiO_2 NWs@rGO benefits from sensitive response to visible light, improved surface re-

* Corresponding authors at: High Level Laboratory of Jiangxi Province for Persistent Pollutants Control, Recycle and Reuse, Nanchang Hangkong University, Nanchang, 330063, PR China.
E-mail addresses: yanglixia829@163.com (L. Yang), sllou@hnu.edu.cn (S. Luo).
[1] The authors contribute equally to this work.

https://doi.org/10.1016/j.jhazmat.2019.120752
Received 15 January 2019; Received in revised form 13 April 2019; Accepted 7 June 2019
Available online 15 June 2019
0304-3894/

activity and high electron flux enabled by rGO and Ti^{3+} in TiO_2. In addition, this composite catalyst can be self–cleaned, and recycled for reuse, which suggests promising potential for waste engine oil treatment.

1. Introduction

Waste engine oil contamination in aquatic systems from marine transportation, oil spills, manufacturing facilities and food processing has caused serious environmental problems [1] such as negative impact on the survival and reproduction of aquatic organisms [2] due to the blocking of light and oxygen penetration by spreading oil layer. It is challenging to remove engine oil from contaminated water because oil is hydrophobic and shows very low affinity to water. Reports abound of removal of waste engine oil are mainly combustion [3], hydro–treatment [4], carbon adsorption [5,6] and biodegradation [7,8]. However, these treatment processes are becoming increasingly impracticable due to secondary pollution, high cost and complex equipment. Therefore, designing a simple, effective and environmentally friendly disposal method to degrade waste engine oil is valuable and challenging.

Recently, numerous reports have been established on photodegradation of organic pollutants due to it's low–cost, safe and environmentally accepted [9,10]. TiO_2, one of the most promising photocatalysts, has been wildly applied in water environmental remediation owing to its high stability and photocatalytic activity under UV irradiation [11,12]. Especially for cationic organic molecules, TiO_2 shows a tendency of adsorbing them due to the high electron density on TiO_2 surface [13]. However, there are two main deficiencies restraining it's application. One is the narrow reactive UV–light spectrum limited by large band gap (3.2 eV), thus causing high cost and energy consumption. The other shortcoming, generally existed in TiO_2 nanoparticles, is the low photoactivity due to the disordered aggregation. In order to broaden its response range to visible light and enable high photocatalytic efficiency, TiO_2 are generally modified with three categories of materials involving narrow–band–gap semiconductor [14,15], noble metals [16,17] and carbon materials [18]. Efficient p/n, p/p or n/n heterojunctions were constructed by combining TiO_2 with semiconductors, with enhanced separation between photoinduced electron–hole pairs [19]. Because degradation generally takes place on photocatalyst surface, sufficient contact between photocatalyst and contaminants determines the final degradation extent. Sometimes, if the pollutants can't be effectively adsorbed by the heterojunction catalyst, no desirable photocatalytic activity can be obtained even though heterojunction can effectively separate charge [20,21]. So, matching one or more semiconductors with high adsorption capacity is necessary. TiO_2 materials modified by noble metals (i.e. Au, Ag and Pd, etc) have achieved relatively mature results. Michael *J*. Nalbandian's group successfully synthesized Ag–TiO_2 composite nanofibers, which showed high photocatalytic activity toward phenol degradation owing to the addition of electron traps and efficient carrier separation [22]. However, the size of noble metals is still a critical determinant of photoreactivity. The cost of noble metals is also an issue. TiO_2 materials modified by carbon materials (i.e. carbon nanotubes and graphene, etc) have become a focus of photocatalysis due to their large surface area, excellent electrical conductivity, acid and alkali resistance and photothermal stability. Among all the carbon materials, graphene has attracted great attention with enlarged surface area and high stability. It has been tentatively applied in the treatment of dyes [23], volatile organic carbons [24], and heavy metals [25]. However, it is not enough to simply remove waste engine oil from water by adsorption. Combining adsorption and simultaneous degradation is required as an effective treatment for engine oil contamination.

In this work, Ti^{3+} self–doped ultra-long TiO_2 nanowires (TiO_2 NWs) were combined with reduced graphene oxide (rGO) to construct composites. Although there are reports about synthesis of TiO_2/graphene composites based on hydrothermal or solvothermal methods [26,27], the combination and application in waste oil removal of ultra-long TiO_2 NWs with Ti^{3+} self-doping and rGO have not been reported up to now. This is the first time employing $NaBH_4$ as reductant which simultaneously realizes the formation of Ti^{3+} dopant in TiO_2 and the reduction of GO. The morphologies and optical properties of as–prepared TiO_2 NWs@rGO composites were rigorously characterized. Experiments of oil adsorption and photocatalytic degradation were conducted to evaluate the performance of TiO_2 NWs@rGO composites. Importantly, a designed fixed–bed reactor using a thin and slight Ti mesh as holder for powder–form TiO_2 NWs@rGO composite showed good recycle and practicability. The detailed degradation processes of waste engine oil involved with reactive oxygen species ($^{\cdot}OH$ and $^{\cdot}O_2$–) generation were investigated. The photocatalytic mechanism of TiO_2 NWs@rGO composites was also presented.

2. Experimental section

2.1. Synthesis of TiO_2 NWs@rGO composites

GO, the precursor of rGO, was prepared by a modified Hummers' method [28]. Then, 0.01 g of GO was added to 15 mL of NaOH (10 mol L^{-1}) solution and stirred for 1 h under 30 rpm. Next, the mixed solution was followed by ultrasonic treatment of 1 h in the ice bath pot (13 °C). Then, 0.1 g of P25 powders (size: 15 nm) and a certain amount of $NaBH_4$ were added to the above solution and stirred for 24 h under 30 rpm in the oil bath pot (130 °C). It is important to keep stirring speed constant (30 rpm) throughout the synthesizing process to ensure the formation and the uniform assembly of elongated TiO_2 over rGO sheets, which is key for high surface areas and fast charge transportation along the longitudinal dimension of TiO_2 NWs@rGO composites [29,30]. After that, the product of hydrothermal reaction was washed 5 times with 300 mL of HNO_3 (0.1 mol L^{-1}) and 200 mL of distilled water in sequence. Finally, the obtained precipitate was dried in a vacuum oven at 60 °C for 12 h and calcined in N_2 atmosphere in a tube furnace at 500 °C for 1 h with heating rate of 2 °C min^{-1}. For differentiation, the TiO_2 NWs@rGO composites prepared at different $NaBH_4$ concentrations (50, 100 and 150 mmolL^{-1}; corresponding weight: 0.028 g, 0.056 g and 0.084 g) were labeled as TiO_2 NWs@rGO–50, TiO_2 NWs@rGO–100 and TiO_2 NWs@rGO–150, respectively. Single TiO_2 nanowires were fabricated by the same way without GO and $NaBH_4$.

2.2. Characterization

The surface morphology of as–prepared samples was observed with field–emission scanning electron microscope (FESEM, Hitachi, S–4800) at 5.0 kV and transmission electron microscope (TEM, JOEL, JEM–2100 F (HR)) at 200 kV. The structure and crystal phase were analyzed by X–ray diffraction (XRD) patterns (MAC Science D/max–3, Cu Kα radiation, λ = 0.154056 nm) and and the first–order Raman spectrum (RENISHAW, RENISHAW–2000). Chemical states of elements were measured by X–ray photoelectron spectroscopy (XPS) using Al–Kα irradiation (Thermo Fisher Scientific, ESCALAB 250). The surface area of synthesized catalyst was determined by Brunauer–Emmett–Teller (BET) adsorption isotherms (MAXON, TriStar II 3020). The photocurrent density of the as–prepared samples was recorded on a electrochemical analyzer (Shanghai Chenhua Instrument Limited Company, CHI660C) irradiated under a 300 W Xe lamp (PerfectLight, PLS–SXE300). The optical property was illustrated by fluorescence spectra (PL, Hitachi, F–7000) and UV–vis diffusion reflectance spectra

(DRS, Hitachi, U–39000H, $BaSO_4$ reference). Fourier transform infrared spectroscopy (FT–IR) were measured by a infrared spectrometer (BRUKER, VERTEX70, KBr reference).

2.3. Photocatalysis experiment

First, simulated seawater system spiked with waste engine oil was prepared as below. 35 g of NaCl was dissolved in 965 mL of deionized water to form simulated sea water with a salinity of 35‰ [31]. Waste engine oil (5 g L^{-1}) collected from the Engineering Training Center of Nanchang Hangkong University (longitude: 115.84 °E, latitude: 28.65 °N) was added to the simulated seawater system at a volume ratio of 1:100 and stirred for 1 h at a speed of 400 rpm. After that, the mixture was placed in a dark place for 2 days.

The photocatalysis experiment was performed in a 100 mL photoreactor filled with simulated seawater system spiked with waste engine oil under simulated solar light from a 300 W Xe lamp (PerfectLight, PLS–SXE300). The distance between the lamp and liquid level was 15 cm. The actual light irradiation reaching the surface of the photocatalyst was 2426.4 mJ cm^{-2} measured by the radiometer (CEAULiGHT, CEL–NP2000) equipped with an electronic sensor. In the experiment, keeping the temperature at 25 °C throughout the experiment. 0.25 g of catalyst was applied in the simulated engine oil–seawater solution and stirred (30 rpm) for 30 min in dark. 1 mL of sampling was taken out before light irradiation in order to assess the adsorption capacity of catalyst. After the photocatalysis started, five samples of 1 mL each were withdrawn from the reactor at light irradiation interval of 1 h. All the samples were saved in dark and analyzed by a COD analyzer (HACH, DR1010) after high–temperature digestion (150 °C, 2 h) in the COD digest instrument (HACH, DRB200).

The stability of catalyst was also assessed through 5 recycling experiments in the same photocatalytic system. The catalyst was separated by water washing and centrifugation (Hitachi, CR22GIII) at a high speed of 8000 rpm after each photocatalytic reaction.

Intermediates and final products from degradation of waste engine oil were also analyzed by gas chromatography–mass spectrometry (GC–MS) for hydrocarbon composition in a GC–MS spectrometer (GC/MS2010, Shimadzu Corp.). The GC–MS spectra (Fig. S1, Supporting information) showed that the waste oil was a mixture of hydrocarbon compounds in the range of C_6–C_{19}. After 5 h photocatalytic degradation, the contents of the compounds of C_6–C_{19} were significantly reduced. Only traces of C_{14} (m/z = 207) and C_{19} (m/z = 281) were detected, demonstrating a decomposition process under irradiation.

3. Results and discussion

3.1. Morphology and structure characterization

Fig. 1 shows the SEM images of the as–prepared samples of TiO_2 NWs and TiO_2 NWs@rGO composites which were synthesized with increased concentrations of $NaBH_4$. Inserts are the digital pictures of corresponding products. Fig.1a depicts the intertwining bundled structure of pristine TiO_2 NWs of 10 μm in length. Fig. 1b shows the morphology of TiO_2 NWs@rGO composite fabricated at 50 mmol L^{-1} $NaBH_4$, which exhibits a mixed form of TiO_2 NWs and poor–quality rGO layers. The same white color of TiO_2 NWs@rGO–50 as TiO_2 NWs suggests the failed formation of rGO. In comparison, thin graphene layers with some winkles are observed in Fig. 1c and d as the concentration of $NaBH_4$ increases. These layers exert a positive effect between NWs and rGO sheets, which not only serve as support for the long TiO_2 NWs, but also form a three dimensional network for electron transfer. Specifically, two–dimensional rGO layers prevent the bundling of TiO_2 NWs, and one–dimensional pristine TiO_2 NWs restrain the stacking of rGO, thus endowing the as–prepared composite with high surface area and superior conductivity [32]. Furthermore, the color of TiO_2 NWs@rGO–100 and NWs@rGO–150 turns deep gray, which is superior to

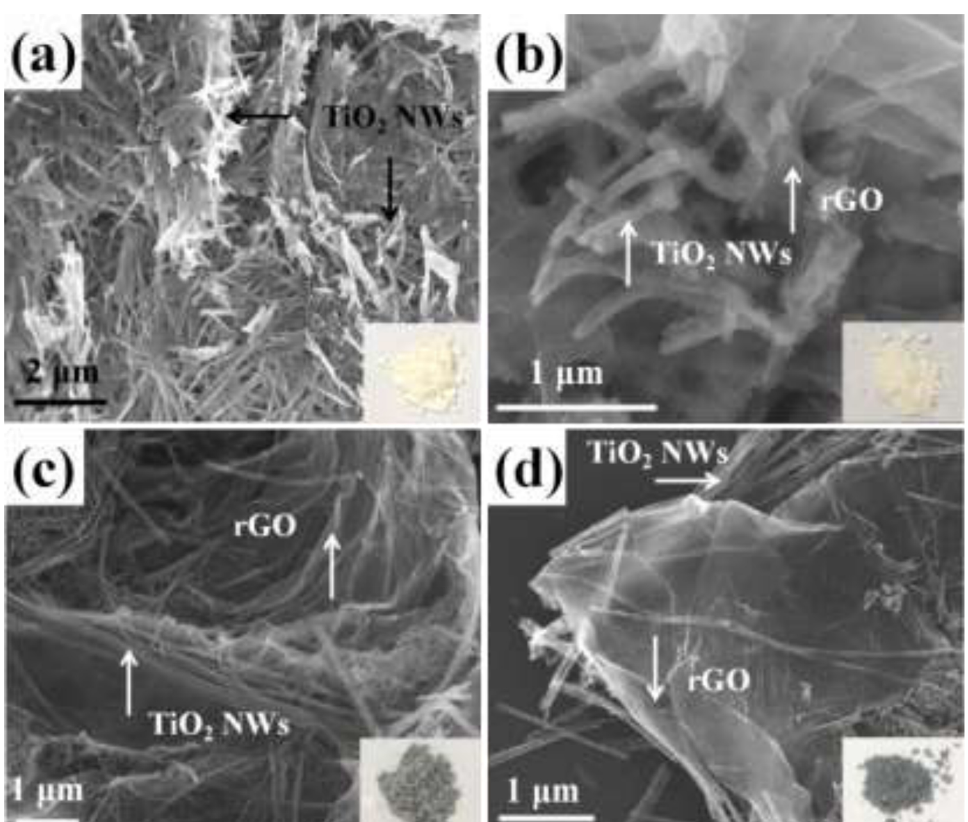

Fig. 1. SEM images of (a) TiO_2 NWs, (b) TiO_2 NWs@rGO–50, (c) TiO_2 NWs@rGO–100 and (d) TiO_2 NWs@rGO–150. Insets show the pictures of catalysts.

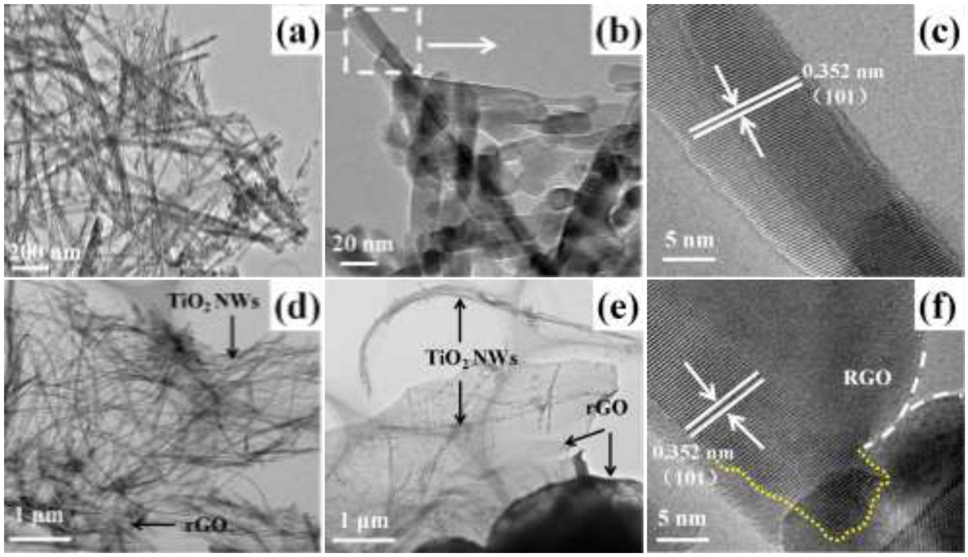

Fig. 2. TEM images of (a) TiO_2 NWs and (d) TiO_2 NWs@rGO–100; Enlarged TEM images of (b) TiO_2 NWs and (c) TiO_2 NWs@rGO–100; HRTEM images of (c) TiO_2 NWs and (f) TiO_2 NWs@rGO–100.

white TiO_2 NWs and TiO_2 NWs@rGO–100 in light absorption.

The TEM and HRTEM images of TiO_2 NWs and TiO_2 NWs@rGO–100 are displayed in Fig. 2. It can be seen from Fig. 2a that the typical curl of TiO_2 NWs are over 10 μm in length and 17 nm in diameter, and the lattice distance assigned to (101) planes of anatase is 0.352 nm (Fig.2b–c) [33]. Because the (101) plane stacks regularly along the growth direction, TiO_2 NWs exhibits high crystallinity and photoactivity. Observed from Fig. 2d–e, TiO_2 NWs grow in situ on the surface of rGO nanosheets, which is further confirmed by the coexistence of anatase NWs and rGO observed in Fig. 2f. It is noteworthy that the edge (marked by yellow line) of the end part in a TiO_2 NW is curving, which illustrates disordered lattice layer there. This can be assigned to Ti^{3+} defect generated from the reduction of Ti^{4+} by $NaBH_4$ [34]. Ti^{3+}, a vital electron capture center, can effectively inhibit the recombination of electron–hole, resulting in enhanced electron utilization and photocatalytic activity [35].

3.2. XRD and Raman spectra of the as–prepared specimen

In Fig. 3a, the XRD patterns of anatase standard, TiO_2 NWs and TiO_2 NWs@rGO–100 are compared. The characteristic peaks of TiO_2 NWs at 25.3°, 37.8°, and 48.2° correspond to the lattice plane of (101), (004) and (200) in anatase standard (JCPDS card No. 21–1272), respectively. The TiO_2 NWs@rGO–100 composite exhibits the same XRD pattern as that of TiO_2 NWs, which is in agreement with the HRTEM analysis in Fig. 2d and 2f, and this suggests that the high photoactivity is probably caused by anatase TiO_2 [36]. However, there is no diffraction peak of graphene for TiO_2NWs@rGO–100, which may be attributed to the low loading content and limited stacking of single–layer graphene [37], but the construction of graphene is successfully observed in Raman spectroscopy in Fig. 3b.

Raman spectroscopy is an effective and sensitive method for identification of the fine structure of carbonaceous material, especially for graphene–based catalyst. As shown in Fig. 3b, there are two significant peaks in rGO and TiO_2 NWs@rGO–100 samples. The peak D at 1330 cm^{-1} corresponds to the sp^3–hybridization of disordered carbon atoms, and the peak G at 1580 cm^{-1} indexes the sp^2–hybridization of ordered carbon atoms [38]. Besides, Raman bands at 388, 495, and 620 cm^{-1} labeled as B_{1g}, A_{1g}/B_{1g}, and E_{g2} are attributed to corresponding anatase modes. Above analysis illustrates that TiO_2 NWs@rGO–100 posses both constructions of rGO and TiO_2.

3.3. XPS analysis

XPS spectra of TiO_2 NWs@rGO–100 are shown in Fig. 4, revealing the dominant elements of TiO_2 NWs@rGO–100 are Ti, O and C. Detailed information identified as Ti 2p, O 1s, and C 1s is depicted in Fig. 4b–d, respectively. In Fig. 4b, the peaks at 458.5 eV and 464.1 eV represents the existence of Ti^{4+}, while the peaks at 457.9 eV and 463.6 eV are assigned to Ti^{3+} [39]. Ti^{3+} ions are the significant defects

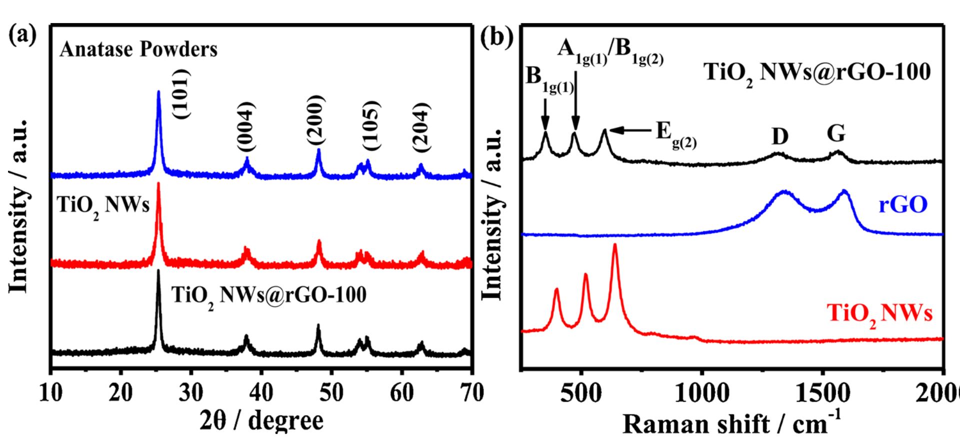

Fig. 3. (a) XRD patterns of anatase powders, TiO_2 NWs and TiO_2 NWs@rGO–100; (b) Raman spectra of TiO_2 NWs, rGO and TiO_2 NWs@rGO–100.

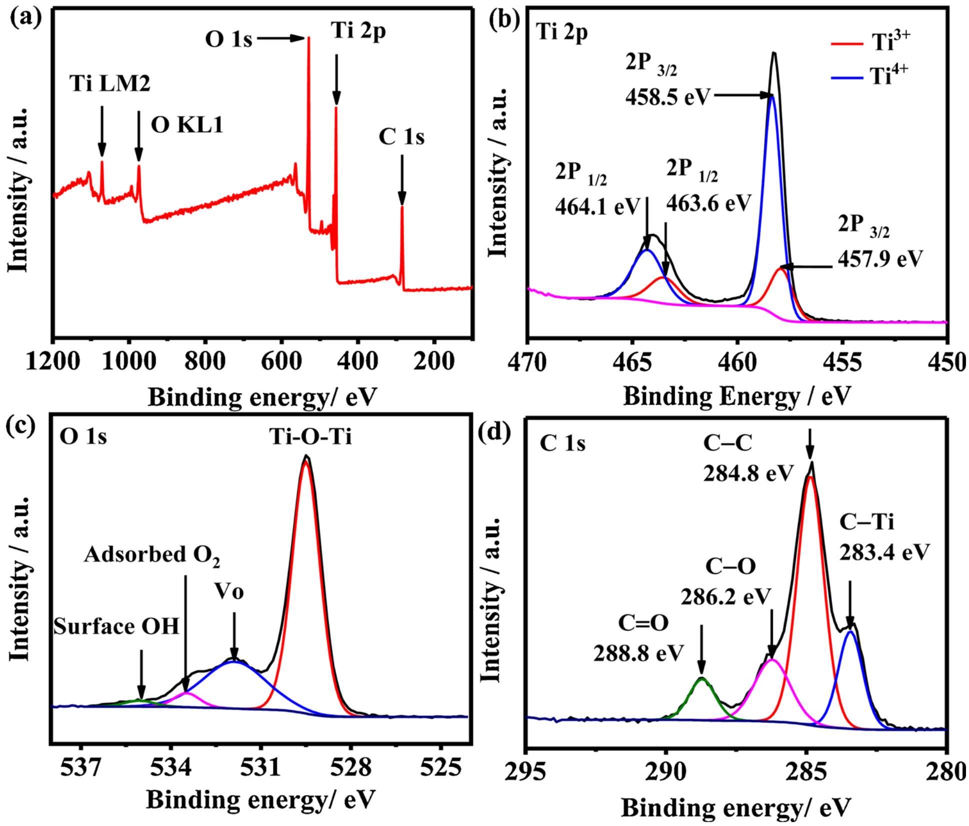

Fig. 4. (a) XPS survey spectrum, (b) Ti 2p core level, (c) O 1s core level and (d) C 1s core level of TiO_2 NWs@rGO–100.

in TiO_2 NWs@rGO–100, which were formed through the reduction of Ti^{4+} by $NaBH_4$ during hydrothermal process. In Fig. 4c, the characteristic peak at 529.5 eV corresponds to Ti–Oi–Ti. The peak at 531.8 eV can be assigned to oxygen vacancy (V_O) [40]. The two peaks at 533.5 eV and 535 eV belong to adsorbed oxygen (O_2) [41] and water molecule (H_2O) [42]. And in Fig. 4d, four peaks at 283.4 eV, 284.8 eV, 286.2 eV and 288.7 eV are assigned to C–Ti, C–C, C–O and C=O band, respectively [43], where C–Ti band results from the coupling between TiO_2 NWs and rGO, and other bands come from rGO.

To further obtain the information of Ti^{3+}, EPR spectra were recorded, as shown in Fig. 5. Under low temperature (77 K), two obvious signals of Ti^{3+} and V_O locate at g = 1.998 and 2.002 [44,45], respectively. The signals of Ti^{3+} and oxygen vacancy (V_O) are very weak in TiO_2 NWs. As for the TiO_2 NWs@rGO composites, TiO_2 NWs@rGO–50, TiO_2 NWs@rGO–100 and TiO_2 NWs@rGO–150 exhibit strong EPR signals of Ti^{3+} and V_O. The higher the concentration of $NaBH_4$, the stronger the EPR signals, which can be assigned to the function from $NaBH_4$.

3.4. BET analysis

In order to determine the specific surface area and pore size for each obtained catalyst, N_2 adsorption–desorption isotherm measurements were carried out. Results displayed in Fig. 6a indicate that the rGO doping remarkably increases the surface area of TiO_2 NWs from 75 m^2 g^{-1} to 116 m^2 g^{-1} for TiO_2 NWs@rGO–50, 182 m^2 g^{-1} for TiO_2 NWs@rGO–100 and 153 m^2 g^{-1} for TiO_2 NWs@rGO–150 due to the interlacement of TiO_2 NWs and graphene sheets. In Fig.6b, it decreases the pore size of TiO_2 NWs from 12.6 nm to 11.4 nm for TiO_2 NWs@rGO–50, 10.2 nm for TiO_2 NWs@rGO–100, and 11.4 nm for TiO_2 NWs@rGO–150 due to the constraint bundling of TiO_2 NWs by rGO layers. This result identifies that as–prepared NWs@rGO composites process high porosity, multilayer and mesoporous structure (Type IV isotherm), which indicates their high adsorptivity.

3.5. Photocurrent response and fluorescence analyses

Photocurrent density of the as–prepared samples was recorded by a CHI660C electrochemical analyzer in a typical three–electrode system using the ITO glass coated with catalyst film (1 cm × 1 cm) as working electrode, a platinum sheet (1 cm × 1 cm) as counter electrode and the saturated calomel electrode (SCE) as reference. Na_2SO_4 solution (50 mL, 0.5 mol/L) was the electrolyte. After the test started, the working electrode was followed by a 300 W Xe lamp (PerfectLight, PLS–SXE300, $\lambda > 420$ nm) radiation with 50s–on–50s–off cycles. As

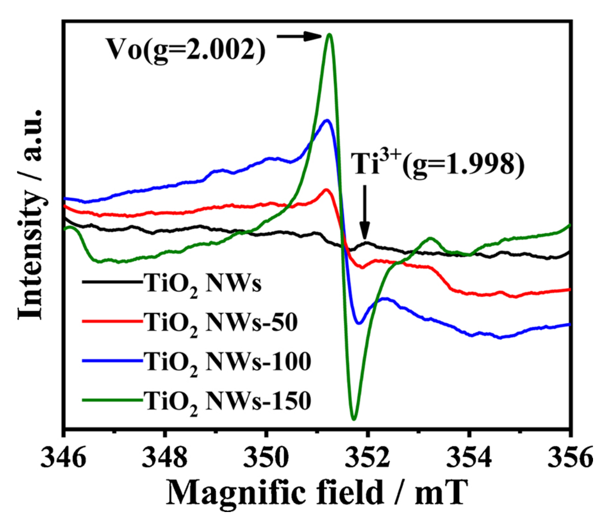

Fig. 5. EPR spectra of TiO_2 NWs, TiO_2 NWs@rGO–50, TiO_2 NWs@rGO–100 and TiO_2 NWs@rGO–150.

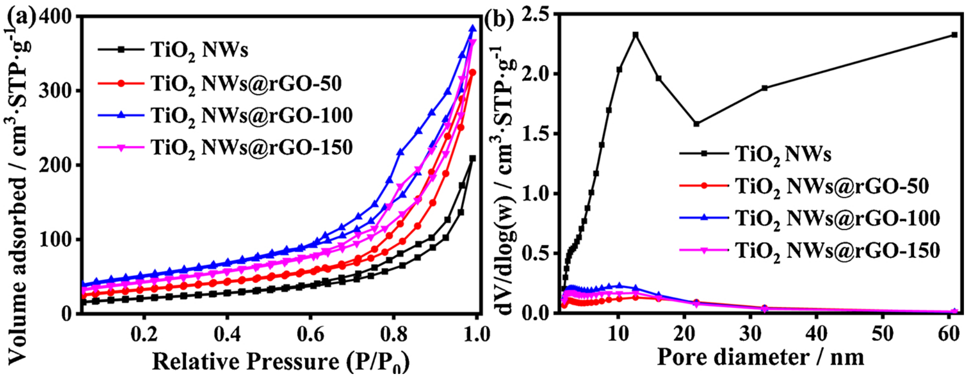

Fig. 6. (a) Adsorption–desorption curves and (b) pore diameter distribution of TiO_2 NWs, TiO_2 NWs@rGO–50, TiO_2 NWs@rGO–100 and TiO_2 NWs@rGO–150.

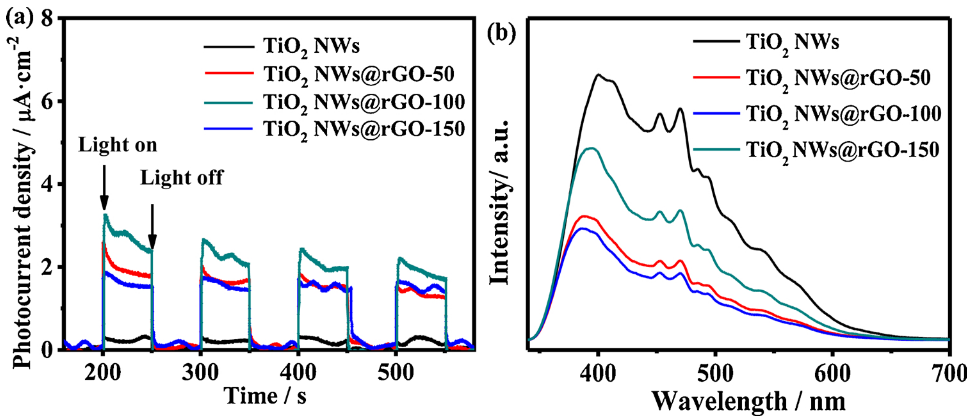

Fig. 7. (a) Photocurrent responses and (b) fluorescence spectra of TiO_2 NWs, TiO_2 NWs@rGO–50, TiO_2 NWs@rGO–100 and TiO_2 NWs@rGO–150.

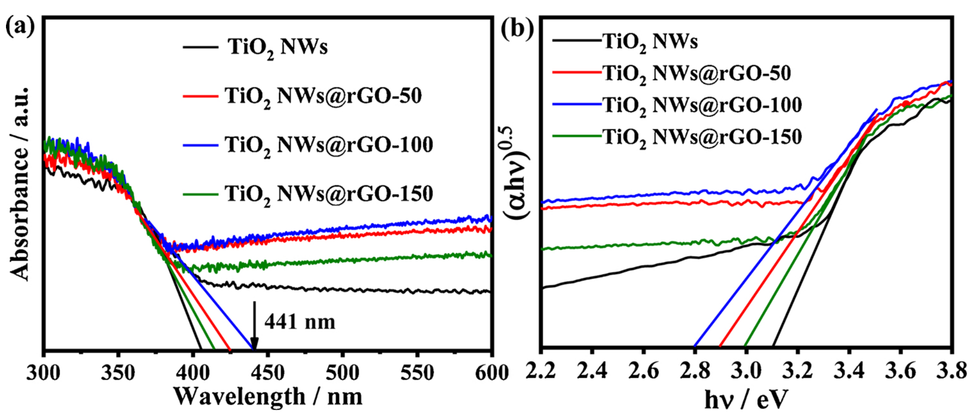

Fig. 8. (a) UV–vis diffuse reflection spectra and (b) plots of transformed Kubelka–Munk function versus the energy of TiO_2 NWs, TiO_2 NWs@rGO–50, TiO_2 NWs@rGO–100 and TiO_2 NWs@rGO–150.

show in Fig. 7a, light irradiation generates different photocurrent density in different catalysts where TiO_2 NWs@rGO composites have higher photocurrent density than that of TiO_2 NWs. The maximum value of 2.6 μA cm^{-2} occurs in TiO_2 NWs@rGO–100, which is 8.7 times higher than that of the TiO_2 NWs (0.3 μA cm^{-2}).

Fig. 7b presents the photoluminescence (PL) spectra of TiO_2 NWs and TiO_2 NWs@rGO composites excited at 320 nm. All the samples have two peaks at 453 nm and 476 nm, which are ascribed to Ti^{3+} and the charge transition from Ti^{3+} to oxygen anion [46], respectively. Because the PL intensity is positively proportioned to the frequency of the recombination between photoinduced electron–hole pairs, and negatively proportioned to photoactivity, the higher the intensity, the faster the recombination, thus the poorer the photoactivity. In Fig. 7b, the PL intensity varying with the change of concentration of $NaBH_4$ achieves the lowest response at NWs@rGO–100, which reveals that rGO combination and Ti^{3+} doping can prevent the recombination of photogenerated carriers.

3.6. DRS and Mott–schottky analyses

The diffuse reflection spectra and Mott–Schottky plots of TiO_2 NWs and TiO_2 NWs@rGO composites were displayed in Fig. 8. In Fig. 8a, compared with TiO_2 NWs, TiO_2 NWs@rGO composites have an obvious red shift of the absorption band edge from 405 nm to 441 nm, which is credited to Ti^{3+} self–doping [47]. And the enhanced light absorption in the range of 400 to 600 nm is due to the intrinsic dark color of rGO. The band gap energy of a semiconductor can be calculated according to Kubelka–Munk function coupled with indirect procedure [48,49]:

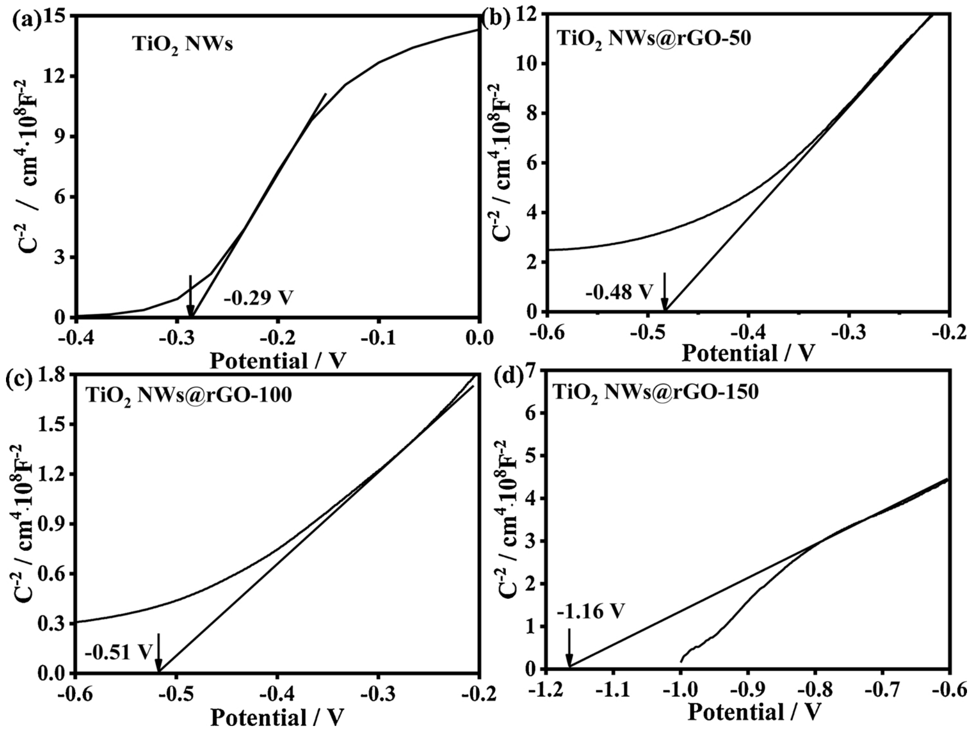

Fig. 9. Mott–Schottky plots of (a) TiO_2 NWs, (b) TiO_2 NWs@rGO–50, (c) TiO_2 NWs@rGO–100 and (d) TiO_2 NWs@rGO–150.

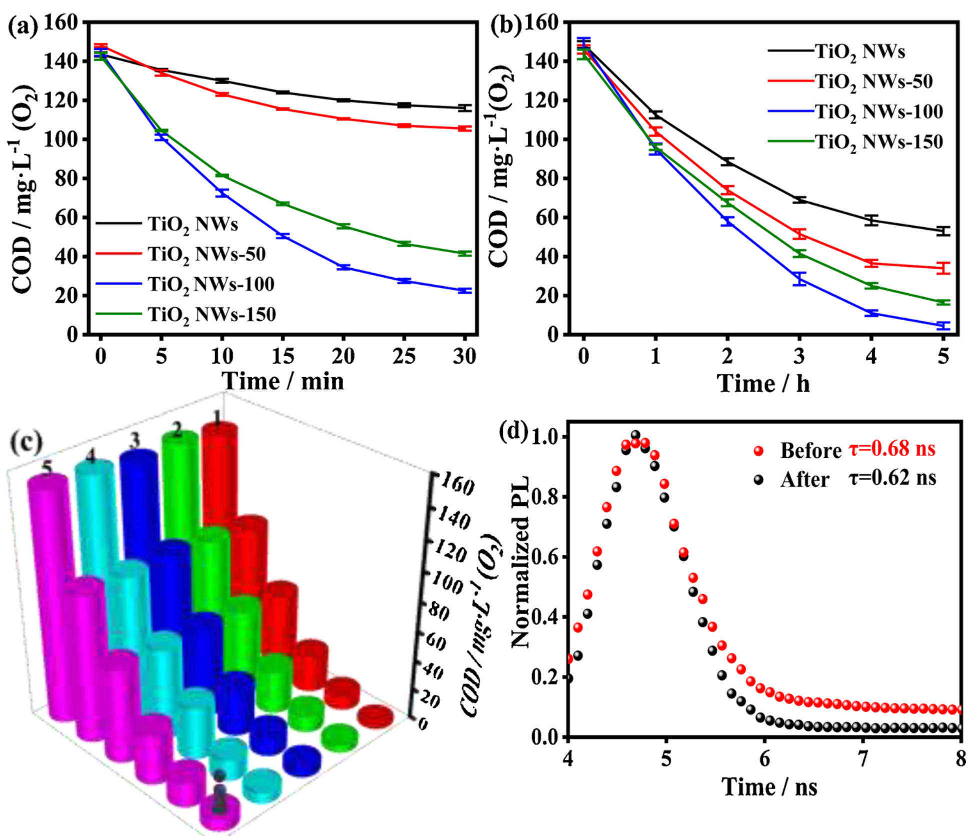

Fig. 10. Decrease of COD in simulated sea water (a) by adsorption (t = 30 min) and (b) adsorption combined with degradation using TiO_2 NWs, TiO_2 NWs@rGO–50, TiO_2 NWs@rGO–100, TiO_2 NWs@rGO–150 (t = 5 h). Each point represents the average of three replicates, and error bars represent single standard deviations. (c) Reusability tests of TiO_2 NWs@rGO–100. (d) Transient PL decay of TiO_2 NWs@rGO–100 before and after 5 cycles.

$$(\alpha * hv)^{0.5} = B(hv - E_g) \quad (1)$$

Where α is the absorption. h is the Planck constant (6.63×10^{-34} Joule s^{-1}). ν is the irradiation frequency. E_g is the band gap energy of nanomaterial (eV), λ_g is the absorption threshold of nanomaterial to light (nm). As shown in Fig. 8b, the optical bandgaps calculated by dropping a line from the maximum slope of the light absorption curve to the x–axis is 3.1 eV for TiO_2 NWs, 3.0 eV for TiO_2 NWs@rGO–150, 2.9 eV for TiO_2 NWs@rGO–50, and 2.8 eV for TiO_2 NWs@rGO–100, respectively.

The influence of $NaBH_4$ dosage on the energy level of TiO_2 NWs@

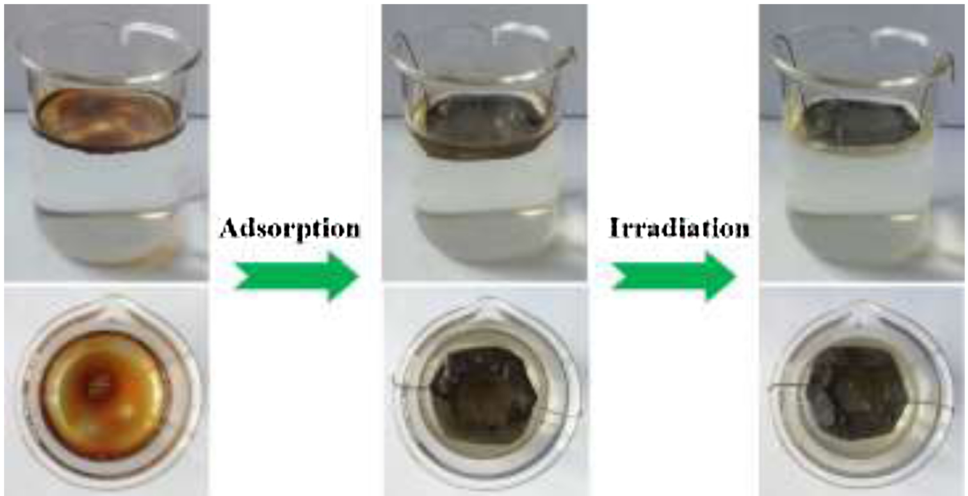

Fig. 11. The changes of a waste engine oil contaminated water sample employing TiO_2 NWs@rGO–100/Ti mesh complex as adsorber and photocatalyst.

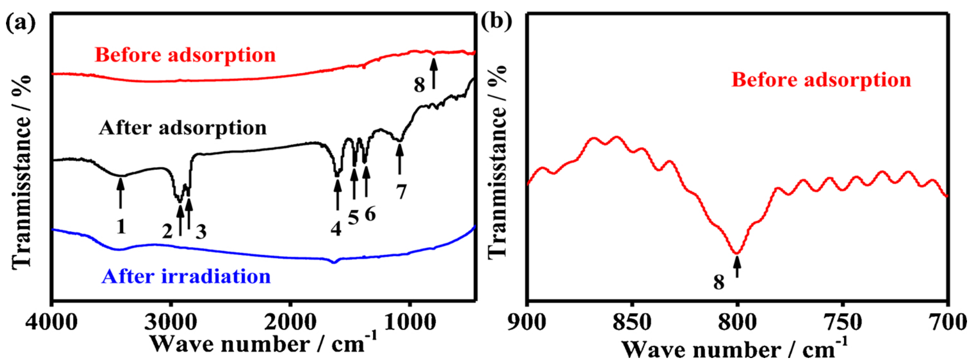

Fig. 12. (a) The IR spectra of TiO_2 NWs@rGO–100 before adsorption, after oil adsorption, and after degradation test for 5 h. (b) The enlarged IR spectra of TiO_2 NWs@rGO–100 before adsorption.

Table 1
Wavenumbers, bonds, and corresponding functional groups demonstrated in Fig. 11.

Number	Wavenumber (cm^{-1})	Bond	Functional Groups
1	3430	−OH	Hydroxyl
2	2930	H antisymmetric stretch	$-CH_2-$
3	2850	C−H symmetric stretch	$-CH_2-$
4	1610	C−O antisymmetric stretch	COO−
5	1460	C−H bending vibration	$-CH_2-$
6	1380	C−H bending vibration	$-CH_3$
7	1080	C−O stretching vibration	R−OH
8	803	Ti−O−C	

rGO composites is evaluated by Mott–Schottky electrochemical analysis. Fig. 9a–d display the Mott–Schottky plots of TiO_2 NWs, TiO_2 NWs@rGO–50, TiO_2 NWs@rGO–100 and TiO_2 NWs@rGO–150. The positive slopes demonstrate that all the samples are n–type semiconductors. The flat–band potential (V_{fb}) can be correspondingly read as –0.29, –0.48, –0.51 and –1.16 V referring to the standard Ag/AgCl electrode, corresponding to be –0.07, –0.26, –0.29 and –0.94 V referring to the Normal Hydrogen Electrode (NHE). There is an obvious negative shift of V_{fb} observed. As for n–type semiconductor, the flat band potential (V_{fb}) is equivalent to its Fermi level (E_f) [50]. The more negative E_f indicates that the stock of photogenerated electrons in TiO_2 NWs@rGO composites is increased as the concentration of $NaBH_4$ increased, and thus during photocatalysis the resulting superoxide radicals ($^{\cdot}O_2–$) generated through O_2 reduction by stocked electrons on the surface of rGO will dominate as reactive species.

3.7. Photocatalytic degradation of waste engine oil

Purification experiments of simulated waste engine oil contamination were conducted to compare the performance of TiO_2 NWs, TiO_2 NWs@rGO–50, TiO_2 NWs@rGO–100 and TiO_2 NWs@rGO–150. Results are presented in Fig. 10. Fig. 10a shows the capacity of four catalysts for engine oil adsorption. It can be seen that TiO_2 NWs@rGO–100 exhibits the highest adsorption capacity of 86% COD removal within 30 min, which is probably attributed to it's highest BET surface area of 182 m^2 g^{-1}. Fig. 10b displays the combined effects of adsorption and photocatalytic degradation. All removal efficiency of waste engine oil is significantly enhanced due to the additional photocatalytic degradation activated by the irradiation. TiO_2 NWs@rGO–100 performs the best with 98.6% removal of COD and 2 mg L^{-1} of final COD.

The stability and reusability of TiO_2 NWs@rGO–100 were also investigated. As shown in Fig. 10c, the COD removal extent in five consecutive cycles is 98.6%, 97.3%, 95.9%, 95.3% and 94.7%, respectively. No obvious decline occurred after five cycles with the same catalyst, demonstrating the high stability of TiO_2 NWs@rGO–100. Furthermore, the carrier lifetime of TiO_2 NWs@rGO–100 before and after 5 cycles was compared to evaluate the stability of photogenerated carriers. In Fig. 10d, the lifetimes τ obtained for TiO_2 NWs@rGO–100 before and after degradation tests are 0.68 ns and 0.62 ns. Low attenuation of carrier lifetime ensures high stability of TiO_2 NWs@rGO–100.

3.8. Design and application of fixed–bed reactor

In terms of practical application, TiO_2 NWs@rGO composite (TiO_2 NWs@rGO–100 as the model catalyst) is spread on the surface of a Ti

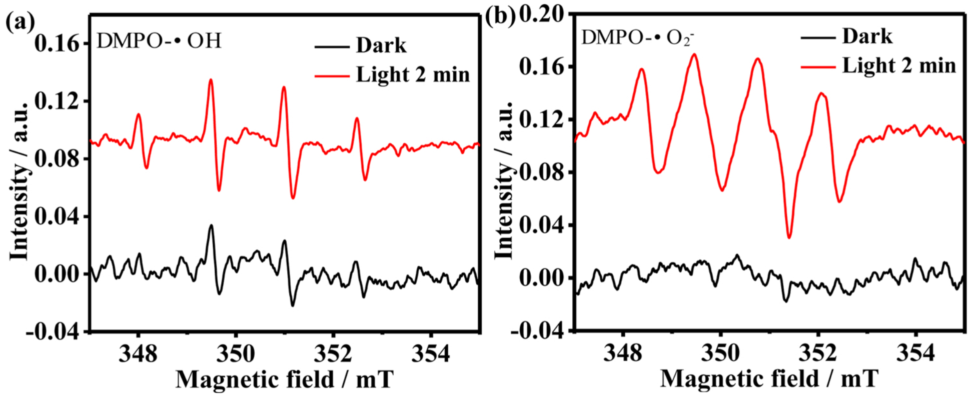

Fig. 13. DMPO spin–trapping ESR spectra for (a) DMPO– ·OH over TiO_2 NWs@rGO–100 in aqueous (b) DMPO– $\cdot O_2{}_-$ in methanol dispersions. [DMPO] = 50 mM, $[SO_3{}^{2-}]$ = 5 mM, catalyst loading = 0.3 g L^{-1}, pH = 7, T = 20 °C. ˙O˙O.

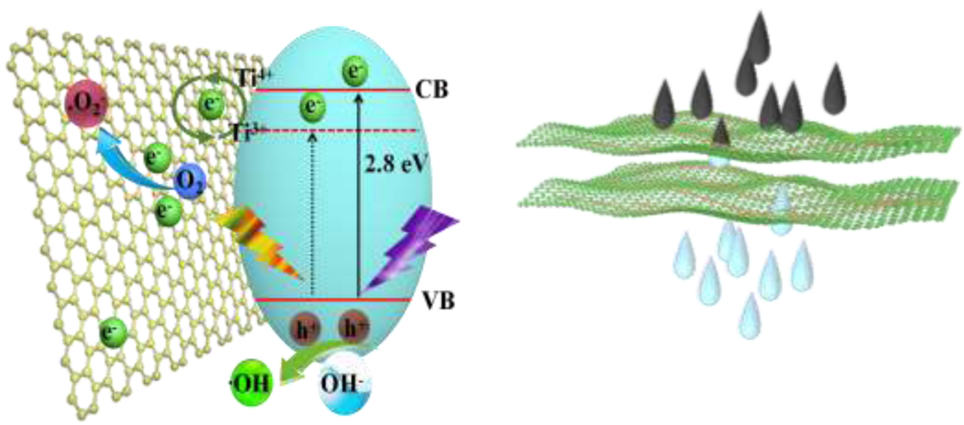

Fig. 14. Schematic electron transfer mechanism over TiO_2 NWs@rGO.

mesh, and other layer of as–prepared Ti mesh is stacked on the former to build one sandwich–structured complex. Fig. 11 exhibits the purification process of a model waste engine oil contaminated water sample employing TiO_2 NWs@rGO/Ti mesh complex as adsorbent and photocatalyst. The waste engine oil initially floats on water, and then migrates towards and accumulates on TiO_2 NWs@rGO/Ti mesh complex gradually once applied, and finally is completely removed from water after photocatalytic degradation for 5 h.

IR spectra were used to analyze chemical bonds and functional groups of substance by recording specific absorption bands [51]. Fig. 12 is the IR spectra of TiO_2 NWs@rGO before process, after oil adsorption, and after degradation test for 5 h. The related characteristic peaks are numbered and noted in Table 1. The result shows that before adsorption (Fig. 12a, red curve) only Ti—O—C bond (zoomed, Fig. 12b) is observed, while after adsorption (Fig. 12a, black curve), characteristic functional groups of engine oil are detected, such as $-CH_2$–, $-CH_3$ and R—OH. Moreover, after photocatalysis, there are no other specific functional groups but COO– left, which means that engine oil is completely mineralized, and that TiO_2 NWs@rGO composite is clean enough for reuse. This result confirms the superior photocatalytic activity as well as self–cleaning property of TiO_2 NWs@rGO composite. In summary, such carefully designed complex is ideal for waste engine oil treatment, because TiO_2 NWs@rGO composite exhibits high adsorption, photocatalytic activity, and sensitive response to visible light; itself can float on water; and its immobilization on Ti mesh besides self–cleaning property makes it easy for recycle and reuse.

3.9. Identification of active species

It is known that ˙OH and ˙O_2– are two conventional active species involved in photocatalysis, which can be detected by electron spin resonance (ESR), thus it is used to identify the active species in the photocatalysis of waste engine oil by TiO_2 NWs@rGO in this study. The obtained ESR spectra using DMPO as the spin–trap are presented in Fig. 13. There is no distinguishable signal generated in dark (black, Fig. 13a, b) while the characteristic spectra of ˙OH (red, Fig. 13a) and ˙O_2– (red, Fig. 13b) are clearly observed after 2 min visible light irradiation. Moreover, the intensity of ˙O_2– is stronger than that of ˙OH, which suggests the fast electron transfer from orientated TiO_2 NWs to graphene for the generation of ˙O_2– on the surface of graphene under visible light irradiation.

3.10. Electron transfer mechanism over TiO_2 NWs@rGO

Based on the above analysis, a possible mechanism of electron transfer in TiO_2 NWs@rGO during photocatalysis is proposed (Fig. 14). First, the irradiation of UV–vis light excites the electron in TiO_2 valence band (VB) to the conduction band (CB). The excited electron can also be trapped by Ti^{3+} and transferred immediately along the nanowire pathway of TiO_2 NWs to the surface of rGO, which can be captured by O_2 to generate ˙O_2– radical [52,53]. This process effectively prevent the recombination of electron–hole pairs [54]. Then, the ˙O_2– reacts with H^+ to generate H_2O_2 and further form ˙OH radical [55]. Attributed to the electron transfer described above, numerous ˙OH radicals are generated and worked as strong oxidants to mineralize the waste engine oil to CO_2 and H_2O. It is noteworthy that the elongated anatase nanowires formed in TiO_2 NWs@rGO enables the orientated pathway of electron transfer which restrains the recombination of electron–hole pairs, and Ti^{3+} doping increases the energy level of TiO_2 in visible light region, resulting in increased yield of photoinduced carriers.

4. Conclusions

The floatable elongated Ti^{3+} doped TiO_2 NWs@rGO composites were synthesized successfully by a facile one–step hydrothermal approach with $NaHB_4$ as reductant, which can effectively remove the floating waste engine oil through adsorption and degradation. The optimal TiO_2 NWs@rGO prepared in the presence 100 mmol L^{-1} $NaHB_4$ exhibits a high surface area of 182 m^2 g^{-1} and high photodegradation extent in removing waste engine oil pollution. The COD of the contaminated water is decreased from 145 mg L^{-1} to 2 mg L^{-1} (98.6% removal extent of COD), which is endowed by the synergistic effect between TiO_2 NWs and rGO layers. Moreover, enhanced harvest to UV–vis light and more negative conduction potential make excited electrons react with O_2 to generate high yield of $^{\cdot}O_2$– and $^{\cdot}OH$ radicals which are responsible for the decomposition of organic chemical. Furthermore, the property of self–cleaning and the immobilization on Ti mesh stack make TiO_2 NWs@rGO composites promising for waste engine oil treatment.

Acknowledgments

This work was financially supported by the National Natural Science Foundation of China (51720105001, 51868051), Key Project of Research and Development Plan of Jiangxi Province (Grant 2016ACG70001), Distinguished Young Scholars Program by Jiangxi Province (Grant 20162BCB23042). All financial support is gratefully.

Appendix A. Supplementary data

Supplementary material related to this article can be found, in the online version, at doi:https://doi.org/10.1016/j.jhazmat.2019.120752.

References

[1] S. Datta, S. Samanta, D. Chaudhuri, Near instantaneous gelation of crude oil using naphthalene diimide based powder gelator, J. Mater. Chem. A Mater. Energy Sustain. 6 (2018) 2922–2926, https://doi.org/10.1039/C7TA10103A.
[2] S. Zhang, G. Jiang, S. Gao, H. Jin, Y. Zhu, F. Zhang, J. Jin, Cupric phosphate nanosheets–wrapped inorganic membranes with superhydrophilic and outstanding anticrude oil–fouling property for oil/water separation, ACS Nano 12 (2018) 795–803, https://doi.org/10.1021/acsnano.7b08121.
[3] M.J. Fuentes, R. Font, M.F. Gómez-Rico, I. Martín-Gullón, Pyrolysis and combustion of waste lubricant oil from diesel cars: decomposition and pollutants, J. Anal. Appl. Pyrol. 79 (2007) 215–226, https://doi.org/10.1016/j.jaap.2006.12.004.
[4] D.W. Brinkman, J.R. Dickson, Contaminants in used lubricating oils and their fate during distillation/hydrotreatment re–refining, Environ. Sci. Technol. 29 (1995) 81–86, https://doi.org/10.1021/es00001a009.
[5] S.S. Lam, R.K. Liew, C.K. Cheng, H.A. Chase, Catalytic microwave pyrolysis of waste engine oil using metallic pyrolysis char, Appl. Catal. B–Environ. 176 (2015) 601–617, https://doi.org/10.1016/j.apcatb.2015.04.014.
[6] N. Nandini, S. Sivasakthivel, Bleaching of sunflower waste oil by absorption on activated carbon and improved by ozonisation, Am. Int. J. Res. Sci. Technol. Eng. Math. (2014) 35–39.
[7] L.B. Salam, Metabolism of waste engine oil by Pseudomonas species, 3 Biotech 6 (2016) 98, https://doi.org/10.1007/s13205–016–0419–5.
[8] H.M. Ibrahim, Biodegradation of used engine oil by novel strains of Ochrobactrum anthropi HM–1 and Citrobacter freundii HM–2 isolated from oil–contaminated soil, 3 Biotech 6 (2016) 226, https://doi.org/10.1007/s13205–016–0540–5.
[9] P. Shao, J. Tian, F. Yang, X. Duan, S. Gao, W. Shi, X. Luo, F. Cui, S. Luo, S. Wang, Identification and regulation of active sites on nanodiamonds: establishing a highly efficient catalytic system for oxidation of organic contaminants, Adv. Funct. Mater. 28 (2018) 1705295, , https://doi.org/10.1002/adfm.201705295.
[10] M. Sun, S. Li, T. Yan, P. Ji, X. Zhao, K. Yuan, D. Wei, B. Du, Fabrication of heterostructured $Bi_2O_2CO_3/Bi_2O_4$ photocatalyst and efficient photodegradation of organic contaminants under visible–light, J. Hazard. Mater. 333 (2017) 169–178, https://doi.org/10.1016/j.jhazmat.2017.03.027.
[11] D. Spanu, S. Recchia, S. Mohajernia, O. Tomanec, S. Kment, R. Zboril, M. Altomare, Templated dewetting–alloying of NiCu bilayers on TiO_2 nanotubes enables efficient noble–metal–free photocatalytic H_2 evolution, ACS Catal. 8 (2018) 5298–5305, https://doi.org/10.1021/acscatal.8b01190.
[12] W.H. Lam, M.N. Chong, B.A. Horri, B.T. Tey, E.S. Chan, Physicochemical stability of calcium alginate beads immobilizing TiO_2 nanoparticles for removal of cationic dye under UV irradiation, J. Appl. Polym. Sci. 134 (2017) 1–8, https://doi.org/10.1002/app.45002.
[13] A. Nezamzadeh–Ejhieh, M. Khorsandi, Heterogeneous photodecolorization of eriochrome black T using Ni/P zeolite catalyst, Desalination 262 (2010) 79, https://doi.org/10.1016/j.desal.2010.05.047.
[14] Z. Xiong, Z. Lei, C.C. Kuang, X. Chen, B. Gong, Y. Zhao, J.C. Wu, Selective photocatalytic reduction of CO_2 into CH_4 over Pt–Cu_2O/TiO_2 nanocrystals: the interaction between Pt and Cu_2O cocatalysts, Appl. Catal. B–Environ. 202 (2017) 695–703, https://doi.org/10.1016/j.apcatb.2016.10.001.
[15] Y. Wei, L. Li, W. Fang, R. Long, O.V. Prezhdo, Weak donor–acceptor interaction and interface polarization define photoexcitation dynamics in the MoS_2/TiO_2 composite: time–domain Ab initio simulation, Nano Lett. 17 (2017) 4038–4046, https://doi.org/10.1021/acs.nanolett.7b00167.
[16] G.K.K. Gunasooriya, E.G. Seebauer, M. Saeys, Ethylene hydrogenation over Pt/TiO_2: a charge–sensitive reaction, ACS Catal. 7 (2017) 1966–1970, https://doi.org/10.1021/acscatal.6b02906.
[17] J. Zhang, B. Wang, E. Nikolla, J.W. Medlin, Directing reaction pathways through controlled reactant binding at Pd–TiO_2 Interfaces, Angew. Chemie Int. Ed. English 56 (2017) 6594–6598, https://doi.org/10.1002/anie.201703669.
[18] J. Low, B. Cheng, J. Yu, Surface modification and enhanced photocatalytic CO_2 reduction performance of TiO_2: a review, Appl. Surf. Sci. 392 (2017) 658–686, https://doi.org/10.1016/j.apsusc.2016.09.093.
[19] H. Derikvandi, A. Nezamzadeh–Ejhieh, Increased photocatalytic activity of NiO and ZnO in photodegradation of a model drug aqueous solution: effect of coupling, supporting, particles size and calcination temperature, J. Hazard. Mater. 321 (2017) 629–638, https://doi.org/10.1016/j.jhazmat.2016.09.056.
[20] A. Nezamzadeh–Ejhieh, S. Khorsandi, Photocatalytic degradation of 4–nitrophenol with ZnO supported nano–clinoptilolite zeolite, J. Ind. Eng. Chem. 20 (2014) 938, https://doi.org/10.1016/j.jiec.2013.06.026.
[21] A. Nezamzadeh–Ejhieh, M. Khorsandi, Photodecolorization of Eriochrome Black T using NiS–P zeolite as a heterogeneous catalyst, J. Hazard. Mater. 176 (2010) 629–637, https://doi.org/10.1016/j.jhazmat.2009.11.077.
[22] M.J. Nalbandian, M. Zhang, J. Sanchez, S. Kim, Y.H. Choa, D.M. Cwiertny, N.V. Myung, Synthesis and optimization of Ag–TiO_2 composite nanofibers for photocatalytic treatment of impaired water sources, J. Hazard. Mater. 299 (2015) 141–148, https://doi.org/10.1016/j.jhazmat.2015.05.053.
[23] K. Im, D.N. Nguyen, S. Kim, H.J. Kong, Y. Kim, C.S. Park, H. Yoon, Graphene–embedded hydrogel nanofibers for detection and removal of aqueous–phase dyes, ACS Appl. Mater. Inter. 9 (2017) 10768–10776, https://doi.org/10.1021/acsami.7b01163.
[24] J. Lee, M. Kang, I.K. Shim, D.H. Lee, A. Kim, H. Jung, Pore parameters–dependent adsorption behavior of volatile organic compounds on graphene–based material, J. Nanosci. Nanotechno. 18 (2018) 6995–7003, https://doi.org/10.1166/jnn.2018.15448.
[25] R. Sahraei, Z.S. Pour, M. Ghaemy, Novel magnetic bio–sorbent hydrogel beads based on modified gum tragacanth/graphene oxide: removal of heavy metals and dyes from water, J. Clean. Prod. 142 (2017) 2973–2984, https://doi.org/10.1016/j.jclepro.2016.10.170.
[26] M. Nawaz, W. Miran, J. Jang, D.S. Lee, One–step hydrothermal synthesis of porous 3D reduced graphene oxide/TiO_2 aerogel for carbamazepine photodegradation in aqueous solution, Appl. Cataly. B: Environ. 203 (2017) 85–95, https://doi.org/10.1016/j.apcatb.2016.10.007.
[27] L. Gu, J. Wang, H. Cheng, Y. Zhao, L. Liu, X. Han, One–step preparation of graphene–supported anatase TiO_2 with exposed {001} facets and mechanism of enhanced photocatalytic properties, ACS Appl. Mater. Inter. 5 (2013) 3085–3093, https://doi.org/10.1021/am303274t.
[28] L. Yang, D. Yan, C. Liu, H. Song, Y. Tang, S. Luo, M. Liu, Vertically oriented reduced graphene oxide supported dealloyed palladium–copper nanoparticles for methanol electrooxidation, J. Power Sources 278 (2015) 725–732, https://doi.org/10.1016/j.jpowsour.2014.12.141.
[29] P. Zhu, A.S. Nair, P. Shengjie, Y. Shengyuan, S. Ramakrishna, Facile fabrication of TiO_2–graphene composite with enhanced photovoltaic and photocatalytic properties by electrospinning, ACS Appl. Mater. Interf. 4 (2012) 581–585, https://doi.org/10.1021/am201448p.
[30] L. Chen, X. Sheng, D. Wang, J. Liu, R. Sun, L. Jiang, X. Feng, High–performance triphase Bio–photoelectrochemical assay system based on superhydrophobic substrate–supported TiO_2 nanowire arrays, Adv. Funct. Mater. 15 (2018) 1483, https://doi.org/10.1002/adfm.201801483.
[31] S. Wang, Y. Liao, H. Yang, X. Wang, J. Wang, Modeling seawater salinity and temperature sensing based on directional coupler assembled by polyimide–coated micro/nanofibers, Pure Appl. Opt. J. Eur. Opt. Soc. Part A 54 (2015) 10286, https://doi.org/10.1364/AO.54.010283.
[32] X.R. Cao, G.H. Tian, Y.J. Chen, J. Zhou, W. Zhou, C.G. Tian, H.G. Fu, Hierarchical composites of TiO_2 nanowire arrays on reduced graphene oxide nanosheets with enhanced photocatalytic hydrogen evolution performance, J. Mater. Chem. A Mater. Energy Sustain. 2 (2014) 4370–4371, https://doi.org/10.1039/C3TA14272H.
[33] G.H. Tian, K. Pan, Y.J. Chen, J. Zhou, X.H. Miao, W. Zhou, R.H. Wang, H.G. Fu, Vertically aligned anatase TiO_2 nanowire bundle arrays: use as Pt support for counter electrodes in dye–sensitized solar cells, J. Power Sources 238 (2013) 350, https://doi.org/10.1016/j.jpowsour.2013.03.184.
[34] W. Fang, M. Xing, J. Zhang, A new approach to prepare Ti^{3+} self–doped TiO_2 via $NaBH_4$ reduction and hydrochloric acid treatment, Appl. Catal. B: Environ. 160 (2014) 240–246, https://doi.org/10.1016/j.apcatb.2014.05.031.
[35] X. Zhang, H. Tian, X. Wang, G. Xue, Z. Tian, J. Zhang, Z. Zou, The role of oxygen vacancy–Ti^{3+} states on TiO_2 nanotubes' surface in dye–sensitized solar cells, Mater. Lett. 100 (2013) 51–53, https://doi.org/10.1016/j.matlet.2013.02.116.
[36] C. Dette, M.A. Pérez–Osorio, S. Mangel, F. Giustino, S.J. Jung, K. Kern, Atomic structure of water monolayer on anatase TiO_2 (101) surface, J. Phys. Chem. C 122

(2018) 11954–11960, https://doi.org/10.1021/acs.jpcc.8b04210.

[37] Y. Zhang, C. Pan, TiO_2/graphene composite from thermal reaction of graphene oxide and its photocatalytic activity in visible light, J. Mater. Sci. 46 (2011) 2622–2626, https://doi.org/10.1007/s10853–010–5116–x.

[38] Y. Zhang, W. Cui, W. An, L. Liu, Y. Liang, Y. Zhu, Combination of photoelectrocatalysis and adsorption for removal of bisphenol A over TiO_2–graphene hydrogel with 3D network structure, Appl. Catal. B: Environ. 221 (2018) 40, https://doi.org/10.1016/j.apcatb.2017.08.076.

[39] Y. Liu, B. Quan, G. Ji, H. Zhang, One–step synthesis of Ti^{3+} doped TiO_2 single anatase crystals with enhanced photocatalytic activity towards degradation of methylene blue, Mater. Lett. 162 (2016) 138–141, https://doi.org/10.1016/j.matlet.2015.09.133.

[40] M. Xu, Y. Chen, J. Qin, Y. Feng, W. Li, W. Chen, J. Zhu, H. Li, Z. Bian, Unveiling the role of defects on oxygen activation and photodegradation of organic pollutants, Environ. Sci. Technol. 52 (2018) 13881, https://doi.org/10.1021/acs.est.8b03558.

[41] J. Han, Y. Kim, H.W. Kim, D.H. Jackson, D. Lee, H. Chang, H.J. Kim, Effect of atomic–layer–deposited TiO_2 on carbon–supported Ni catalysts for electrocatalytic glycerol oxidation in alkaline media, Electrochem. commun. 83 (2017) 46–50, https://doi.org/10.1016/j.elecom.2017.08.023.

[42] M.M. Viana, N.D.S. Mohallem, D.R. Miquita, K. Balzuweit, E. Silva–Pinto, Preparation of amorphous and crystalline Ag/TiO_2 nanocomposite thin films, Appl. Surf. Sci. 265 (2013) 130–136, https://doi.org/10.1016/j.apsusc.2012.10.151.

[43] Q. Huang, S. Tian, D. Zeng, X. Wang, W. Song, Y. Li, C. Xie, Enhanced photocatalytic activity of chemically bonded TiO_2/graphene composites based on the effective interfacial charge transfer through the C–Ti bond, ACS Catal. 3 (2013) 1477–1485, https://doi.org/10.1021/cs400080w.

[44] Q. Zhang, Y. Yan, G. Chen, A biomineralization strategy for 'Net'-like interconnected TiO_2 nanoparticles conformably covering reduced graphene oxide with reversible interfacial lithium storage, Adv. Sci. 2 (2015) 1500176, , https://doi.org/10.1002/advs.201500176.

[45] J. Zhuang, Q. Tian, Q. Liu, P. Liu, X. Cui, Y. Li, M. Fan, New insight into binary TiO_2@C nanocomposites: the crucial effect of an interfacial microstructure, Phys. Chem. Chem. Phys. 19 (2017) 9519–9527, https://doi.org/10.1039/C7CP00098G.

[46] H. Khan, I.K. Swati, Fe^{3+}–doped anatase TiO_2 with d–d transition, oxygen vacancies and Ti^{3+} centers: synthesis, characterization, UV–vis photocatalytic and mechanistic studies, Ind. Eng. Chem. Res. 55 (2016) 6619–6633, https://doi.org/10.1021/acs.iecr.6b01104.

[47] M. Xing, X. Li, J. Zhang, Synergistic effect on the visible light activity of Ti^{3+} doped TiO_2 nanorods/boron doped graphene composite, Sci. Rep. 4 (2014) 5493, https://doi.org/10.1038/srep05493.

[48] Z. Khodami, A. Nezamzadeh–Ejhieh, Investigation of photocatalytic effect of ZnO–SnO_2/nano clinoptilolite system in the photodegradation of aqueous mixture of 4–methylbenzoic acid/2–chloro–5–nitrobenzoic acid, J. Molecul. Catal. A: Chem. 409 (2015) 62, https://doi.org/10.1016/j.molcata.2015.08.013.

[49] J. Esmaili–Hafshejani, A. Nezamzadeh–Ejhieh, Increased photocatalytic activity of Zn(II)/Cu(II) oxides and sulfides by coupling and supporting them onto clinoptilolite nanoparticles in the degradation of benzophenone aqueous solution, J. Hazard. Mater. 316 (2016) 194–203, https://doi.org/10.1016/j.jhazmat.2016.05.006.

[50] S.S. Patil, N.L. Tarwal, H.M. Yadav, S.D. Korade, T.S. Bhat, A.M. Teli, P.S. Patil, Photoelectrochemical performance of dye and semiconductor sensitization on 1–d hollow hexagonal ZnO rods: a comparative study, J. Solid State Electrochem. 10 (2018) 7–9, https://doi.org/10.1007/s10008–018–3995–y.

[51] A.G. Al–Sehemi, A. Irfan, A.M. Asiri, Y.A. Ammar, Synthesis, characterization and DFT study of methoxybenzylidene containing chromophores for DSSC materials, Spectrochim. Acta A: Mol. Biomol. Spect. 91 (2012) 242, https://doi.org/10.1016/j.saa.2012.01.016.

[52] M. Babaahamdi–Milani, A. Nezamzadeh–Ejhieh, A comprehensive study on photocatalytic activity of supported Ni/Pb sulfide and oxide systems onto natural zeolite nanoparticles, J. Hazard. Mater. 318 (2016) 297, https://doi.org/10.1016/j.jhazmat.2016.07.012.

[53] H. Derikvandi, A. Nezamzadeh–Ejhieh, Synergistic effect of p–n heterojunction, supporting and zeolite nanoparticles in enhanced photocatalytic activity of NiO and SnO_2, J. Colloid Interf. Sci. 490 (2017) 314–327, https://doi.org/10.1016/j.jcis.2016.11.069.

[54] P. Mohammadyari, A. Nezamzadeh–Ejhieh, Supporting of mixed ZnS–NiS semiconductors onto clinoptilolite nano–particles to improve its activity in photodegradation of 2–nitrotoluene, RSC Adv. 5 (2015) 75304, https://doi.org/10.1039/C5RA12608H.

[55] D. Xu, D. Liu, B. Wang, C. Chen, Z. Chen, D. Li, M.G. Kong, In situ OH generation from O_2^- and H_2O_2 plays a critical role in plasma–induced cell death, PLoS One 10 (2015) e0128205,, , https://doi.org/10.1371/journal.pone.0128205.